

Article

Occlusion Culling for Wide-Angle Computer-Generated Holograms Using Phase Added Stereogram Technique

Juan Martinez-Carranza ^{*}, Tomasz Kozacki, Rafał Kukolowicz , Maksymilian Chlipala and Moncy Sajeev Idicula 

Faculty of Mechatronics, Warsaw University of Technology, 8 Sw. A. Boboli Street, 02-525 Warsaw, Poland; t.kozacki@mchtr.pw.edu.pl (T.K.); rafal.kukolowicz.dokt@pw.edu.pl (R.K.); M.Chlipala@mchtr.pw.edu.pl (M.C.); moncy.idicula.dokt@pw.edu.pl (M.S.I.)

* Correspondence: j.martinez@mchtr.pw.edu.pl

Abstract: A computer-generated hologram (CGH) allows synthetizing view of 3D scene of real or virtual objects. Additionally, CGH with wide-angle view offers the possibility of having a 3D experience for large objects. An important feature to consider in the calculation of CGHs is occlusion between surfaces because it provides correct perception of encoded 3D scenes. Although there is a vast family of occlusion culling algorithms, none of these, at the best of our knowledge, consider occlusion when calculating CGHs with wide-angle view. For that reason, in this work we propose an occlusion culling algorithm for wide-angle CGHs that uses the Fourier-type phase added stereogram (PAS). It is shown that segmentation properties of the PAS can be used for setting efficient conditions for occlusion culling of hidden areas. The method is efficient because it enables processing of dense cloud of points. The investigated case has 24 million of point sources. Moreover, quality of the occluded wide-angle CGHs is tested by two propagation methods. The first propagation technique quantifies quality of point reproduction of calculated CGH, while the second method enables the quality assessment of the occlusion culling operation over an object of complex shape. Finally, the applicability of proposed occlusion PAS algorithm is tested by synthetizing wide-angle CGHs that are numerically and optically reconstructed.



Citation: Martinez-Carranza, J.; Kozacki, T.; Kukolowicz, R.; Chlipala, M.; Idicula, M.S. Occlusion Culling for Wide-Angle Computer-Generated Holograms Using Phase Added Stereogram Technique. *Photonics* **2021**, *8*, 298. <https://doi.org/10.3390/photonics8080298>

Received: 2 July 2021

Accepted: 23 July 2021

Published: 27 July 2021

Publisher's Note: MDPI stays neutral with regard to jurisdictional claims in published maps and institutional affiliations.



Copyright: © 2021 by the authors. Licensee MDPI, Basel, Switzerland. This article is an open access article distributed under the terms and conditions of the Creative Commons Attribution (CC BY) license (<https://creativecommons.org/licenses/by/4.0/>).

Keywords: computer-generated hologram; phase added stereogram algorithm; occlusion; frequency domain; Fourier transform; propagation method; wide-angle view; direct integration method; tiling

1. Introduction

The aim of 3D display technology is to reproduce the depth perception of surrounding world. An important feature that must be considered in this technology is the ability to reproduce image providing a complete 3D experience to the viewers [1], i.e., full-parallax. Among several solutions that have been proposed in the last decades for developing 3D display technology, digital holography constitutes the best-known framework due to the ability of truly reconstructing the 3D wavefront [2]. The possibility of complex wavefront reproduction makes digital holography popular choice in several areas as microscopy [3], metrology [4], non-destructive sensing [5], security [6], design of diffractive optical elements [7]. In the realm of display technology, digital holography enables accurate reproduction of physiological cues [8,9], which is important for photorealistic 3-D images. However, digital holographic systems cannot capture scenes for wide-angle viewing display. With the development of computing technology, holograms can be registered without the necessity of a physical holographic setup. Computer-generated hologram (CGH) does not have limitations of physical systems [10] such as optical aberrations, extension, noise, or sensitivity to vibrations. Nevertheless, CGHs have limitations for providing the truly 3D experience. The first limitation is related with the pixel pitch of the spatial light modulators (SLMs) that are used for displaying CGHs. To have a full-parallax, pixel pitches below one micrometer must be used. High-end SLM technologies can offer SLMs with pixel pitch up to 3.74 μm and 4K resolution. Devices in research stage have shown that the pixel pitch

can be reduced up to one micrometer [11,12]. However, this type of technology is still developing. Fortunately, pixel pitch of an SLM can be reduced indirectly by employing optical systems [13], which solves the problem of wide-angle view. The second limitation of CGHs is related to generation of the necessary visual cues for reconstructing photorealistic 3-D images, such as shading, occlusions, transparency, texture mapping, light reflectance properties [14–18]. An important visual cue that any CGH technique must consider is occlusion because it provides information about perception of depth [16]. Implementation of occlusion is a challenging task in CGH since the whole information of a 3D object is coded in 2D hologram. A large variety of occlusion algorithms have been designed depending on the employed CGH technique [16,17,19–22]. Propagation-based CGH techniques can apply occlusion culling of unseen regions [13,17,21,23,24].

A popular approach for obtaining CGHs is employing point clouds of 3D objects. Each point in the cloud act as a point source that is well localized in space with a defined amplitude. Point sources emit a spherical wavefront that propagates to the hologram plane. Superposition of all propagated wavefronts generates the CGH [25–28]. However, occlusion processing for cloud point methods is not a simple task. There are several solutions that can solve this problem. For example, reference [21] employs inter-wave-recording-plane light propagation and masks, which has proved to be efficient. Other researches use the stereogram holographic approach to cull hidden back points [8,29]. A simple technique, called spatial frequency index (SFI), is presented in reference [29]. This approach calculates the instantaneous frequencies of the points with respect to the corresponding hologram tile. Instantaneous frequencies are group in sets of the same frequency, which provides the corresponding occlusion relation with the object points. Finally, the point in the set that is closer to the hologram plane is the only candidate to apport holographic information to the CGH. The SFI method can be understood as a phase added stereogram (PAS) algorithm [30–32] that enables occlusion culling. However, the SFI strategy is time consuming, because it does not employ Fourier transformation (FT). Instead, it uses tables for grouping and selecting the proper frequencies, and what is more important, the size of the tiling is small.

All mentioned approaches enable occlusion culling of unseen areas. However, none of these techniques consider the wide projection angle. For example, propagation-based occlusion techniques are not optimal for CGHs with wide-angle, since they do not usually consider geometry where the object is much larger than the hologram [25]. This geometrical feature is challenging for rigorous propagation algorithms that must be used. For point-occlusion based methods, the wide-angle problem is not considered. In this work, we propose a methodology for occlusion culling based on the Fourier type-PAS algorithm. Unlike the SFI strategy, our approach does not require tables for grouping the corresponding frequencies, and we provide the condition for selecting the sub-hologram tile size for carrying out proper occlusion culling. This allows reducing the processing time of the CGH. The proposed occlusion-PAS-based algorithm enables fast calculation of wide-angle CGHs with the removal of hidden surfaces, which has not been shown until now. The developed PAS method is tested for wide-angle CGH, i.e., small pixel pitch. Moreover, two propagation solutions are proposed for testing the accuracy and quality of the occlusion-based PAS algorithm. The first, based on the direct integration method [33], quantifies quality of point reproduction of calculated CGH. The second, which is a generalization of the multi Fast Fourier Transform Angular Spectrum (MFFT-AS) method [10], assesses the quality of the occlusion culling operation over a 3D object assembled of 24 million of point sources. Theoretical capabilities of our solutions are tested for proving accuracy of computations. Finally, the applicability of our occlusion culling method is carried out numerically and experimentally.

2. Synthesizing CGH with the PAS

A hologram H is obtained as the result of measuring the intensity that results from the linear superposition of a diffracted object wavefield O and a reference wavefield R . The detected intensity can be mathematically expressed as follows

$$H = |O|^2 + |R|^2 + OR * + O * R. \quad (1)$$

The hologram is a set of dark and bright fringes that encode amplitude and phase information of the object. When using a digital camera for registering H , a digital hologram (DH) is obtained. DH can be processed numerically for reconstructing the encoded object information. However, capturing of DHs requires interferometric systems that are sensitive to optical aberrations, environmental and mechanical vibrations, or noise.

With the development of computing technology, holograms can be registered without the necessity of a physical holographic setup. When synthesizing CGH, only the object wave field O is calculated. Solutions for calculating this wavefield have been studied for more than three decades [30,34–37]. The most popular approach consists in decomposing the 3D object into a set of illuminating point sources that are distributed in space. Each point source emits a spherical wavefront that propagates to the hologram plane. Superposition of all propagated wavefronts generate the CGH as follows

$$O = \sum_{p=1}^N \frac{a_p}{D_p} e^{ikD_p}, \quad (2)$$

where $D_p = \sqrt{(x_2 - x_p)^2 + (y_2 - y_p)^2 + z_p^2}$, (x_p, y_p, z_p) are the spatial position and a_p amplitudes of the point sources, respectively. Nevertheless, this solution is time consuming [26,28]. Efficient techniques based on propagation have been proposed for calculating O [21,25,36,38,39]. With the aim to give the viewer a complete 3-D experience with full-parallax, wide-angle CGHs are required. The scheme of geometry for recording wide-angle CGHs is presented in Figure 1. The distance between hologram plane (x_1, y_1) and object plane (x_2, y_2) is z . Field of View (FoV) in a CGH is calculated as $\text{FoV} = 2\sin^{-1}(\lambda/2\Delta)$, where λ and Δ are the wavelength and pixel pitch of the hologram, respectively. Thus, wide-angle CGHs are obtained by employing small pixel pitch at the hologram plane. For example, for given $\lambda = 0.64 \mu\text{m}$ and $\Delta = 0.62 \mu\text{m}$ the $\text{FoV} \approx 62^\circ$. Large FoV allows synthetizing CGHs of objects with spatial extension $B_{x2} = B_{y2} = 2z \tan(\text{FoV})$. These spatial extensions are much larger than the CGH size; for example, when using $z = 1000 \text{ mm}$, $B_{x2} = B_{y2} = 1209 \text{ mm}$ while an a 4K CGH (4120×2060) will have the dimensions $B_{x1} = 2.6 \text{ mm}$ and $B_{y1} = 1.3 \text{ mm}$.

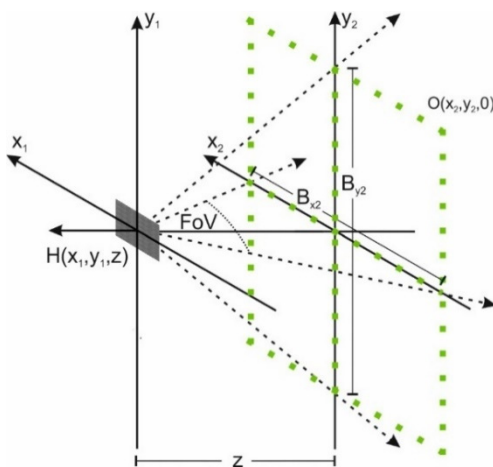


Figure 1. Geometry for recording wide-angle CGHs.

Unfortunately, propagation-based techniques are not an optimal approach for synthetizing CGHs of wide-angle, since they do not consider geometry, where the object is much larger than the hologram [25]. This geometrical feature is challenging for rigorous propagation algorithms. Alternatives for efficient synthesis of CGHs are PAS-based solutions. These solutions do not have the restrictions of propagation-based methods since they consider the basic idea of summing point source responses at the hologram plane [28,31,32]. The PAS algorithm divides the CGH into smaller segments of size $N_s \times N_s$. The number of segments within the CGH is $N \times M$, where N is the number of segments in the horizontal direction and M in the vertical direction. At each segment, PAS approximates the spherical wavefront that comes from the p -th point source of the object with a local tilted plane wave [31], as shown in Figure 2a. The direction of the plane wave is calculated according to the value of the local instantaneous frequency at the center of the segment (x_c^n, y_c^m) , where $n = 1, \dots, N$, and $m = 1, \dots, M$ indicates segment position over the horizontal and vertical direction, respectively. Since the frequency information of each segment is coded according to the local approximation of the tilted plane, the PAS can calculate the diffracted field of objects larger than the hologram size. The term O for a given segment (m,n) is calculated with the PAS as follows

$$O_{mn} = \sum_{p=1}^N \frac{a_p}{D_{pmn}} e^{ikD_{pmn}} \exp(i2\pi[f_{pxnm}(x_1 - x_c^n) + f_{pynm}(y_1 - y_c^m)]), \quad (3)$$

where D_{pmn} is the distance from p -th point source to the center of the segment (m,n) , and

$$f_{pxnm} = \frac{\sin \theta_{pxnm} - \sin \theta_{rxnm}}{\lambda}, \quad (4)$$

$$f_{pynm} = \frac{\sin \theta_{pynm} - \sin \theta_{rynm}}{\lambda}, \quad (5)$$

are the local instantaneous frequencies. The angles θ_{pxnm} , θ_{pynm} , θ_{rxnm} , and θ_{rynm} are the incident angles of object and reference beams on x -axis and y -axis in relation to the center of the segment, respectively. Notably, the hologram in the corresponding segment is a superposition of plane waves. When the reference beam has a constant incident angle, spatial frequencies depend on the object beam [31].

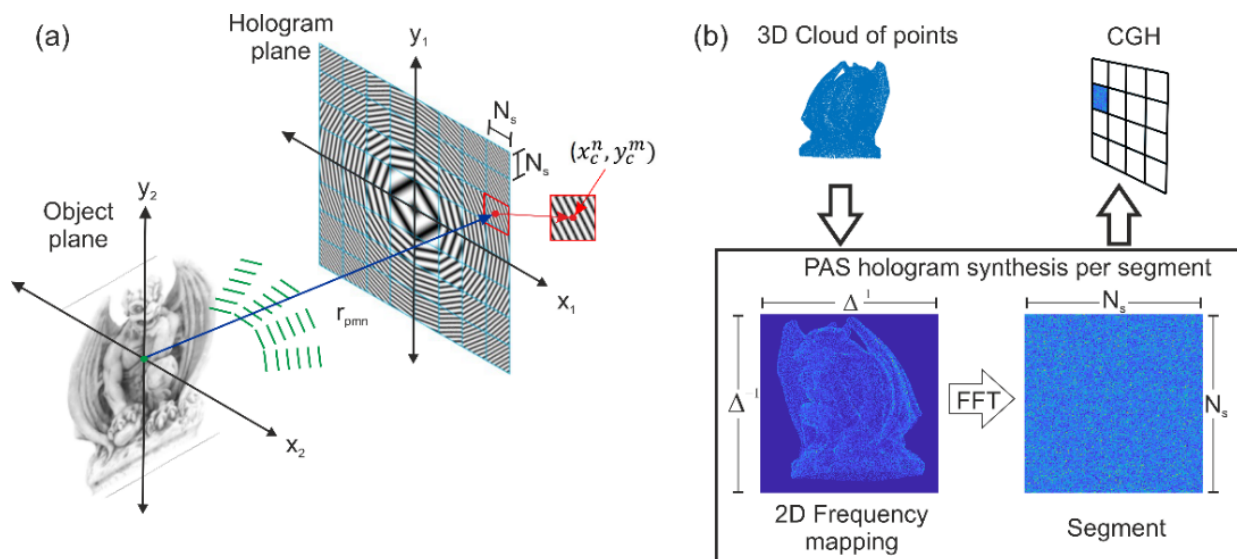


Figure 2. CGH PAS scheme. (a) Spherical wavefront decomposition. (b) CGH synthesis.

Direct computation of Equation (3) can still be slow for a dense cloud of points. Nevertheless, this process can be significantly accelerated when employing the FT. When representing Equation (3) in frequency domain, the plane waves in the segment are transformed into a 2D distribution of Dirac deltas. The positions of these deltas need to be set to a discrete value that is specified by the segment size. Hence, Equations (4) and (5) are rewritten as:

$$\hat{f}_{pxnm} = \left\lfloor \frac{1}{\Delta f} \left(\frac{\sin \theta_{pxnm} - \sin \theta_{rxnm}}{\lambda} \right) \right\rfloor \Delta f, \quad (6)$$

$$\hat{f}_{pynm} = \left\lfloor \frac{1}{\Delta f} \left(\frac{\sin \theta_{pynm} - \sin \theta_{rynm}}{\lambda} \right) \right\rfloor \Delta f, \quad (7)$$

where $\Delta f = 1/N_s \Delta$ is the frequency sampling, and $\lfloor \cdot \rfloor$ is the rounding operation. When employing Equations (6) and (7), the term O_R is expressed in the frequency domain as

$$\hat{O}^{mn} = \sum_{p=1}^N \frac{a_p}{D_{pmn}} \delta(f_x - \hat{f}_{pxnm}, f_y - \hat{f}_{pynm}) e^{ikD_{pmn}}. \quad (8)$$

After placing all the Dirac deltas for the 3D point distribution into the segment, the inverse FT is applied, and then the complex field for a given segment is obtained. This procedure is repeated for all segments for obtaining the CGH, as shown in Figure 2b.

3. Occlusion Culling of Back Points with the PAS

Representation of 3D object for point-based approach offers a simple and flexible way of depicting its shape. Moreover, this representation allows associating the sources with additional information such as colors, textures, and normals [40]. Each point source generates a complex field from the scene towards the hologram plane, and the final CGH is the sum of all corresponding spherical waves. In the point-based representation, point sources cannot occlude one another, unless they accidentally fall along the same direction from the viewpoint. The wavefields from back and front points are encoded in the CGH. This prevents correct reproduction of depth cues of the 3D object in holographic image. In order to eliminate the back points, occlusion techniques are needed. Occlusion techniques can rely on geometric considerations [40], light shielding [17], or hybrid [15,23]. Since the CGH must provide motion parallax, the chosen occlusion technique must consider that the visibility of object changes according to the movement of the viewer.

Occlusion can be introduced by employing the segmentation property of the PAS [29]. As shown in Equation (3), the term O for a given segment (m,n) is a superposition of plane waves having directional wave vectors calculated according to the center of the segment. When applying the FT to the segment, the coordinates of 3D point sources are mapped into the sets of 2D Dirac deltas in frequency domain. The frequency support of this segment is given by Δ^{-1} . Since frequency allocation depends on the size of the segment, the gaps between adjacent Dirac deltas can be controlled in the frequency domain by the value of N_s . Figure 3 illustrates this effect for three point sources when using different segments sizes. The point sources x_p , and x_{p+1} are adjacent front points, while x_m is a back point. The angles of corresponding plane waves are θ_p , θ_{p+1} , and θ_m , respectively. In this example, the angles fulfill the relation $\theta_p < \theta_m < \theta_{p+1}$. Figure 3a presents the case of a small segment. In this case, the wavefront information for all point sources is located in the same frequency pixel since $\hat{f}_p = \hat{f}_{p+1} = \hat{f}_m$. For carrying out the occlusion, information related with the point source x_m needs to be disregarded because it has the farthest separation from the hologram plane. When enlarging the segment, as shown in Figure 3b, wavefront information of front points x_p and x_{p+1} is allocated in frequency pixels \hat{f}_p and \hat{f}_{p+1} , respectively. In this case, the information related to the source x_m will be placed to the nearest neighbor \hat{f}_{p+1} . Similarly to Figure 3a, the information related to the source x_m needs to be disregarded for the occlusion culling. Finally, for large segment the wavefront information of each point source is stored in independent pixels, as presented in Figure 3c. As seen in Figure 3, the

key point of occlusion culling when using PAS is the allocation of frequency information of the sources that are closer to the hologram plane first, which are labeled as front sources. These sources contribute the proper object information to the CGH. Other point sources of the same frequency but farther from the hologram plane are labeled as back sources, which must be disregarded. Thus, sorting of the cloud in respect to the z-axis allows identifying points from the nearest to the farthest in respect to the hologram plane.

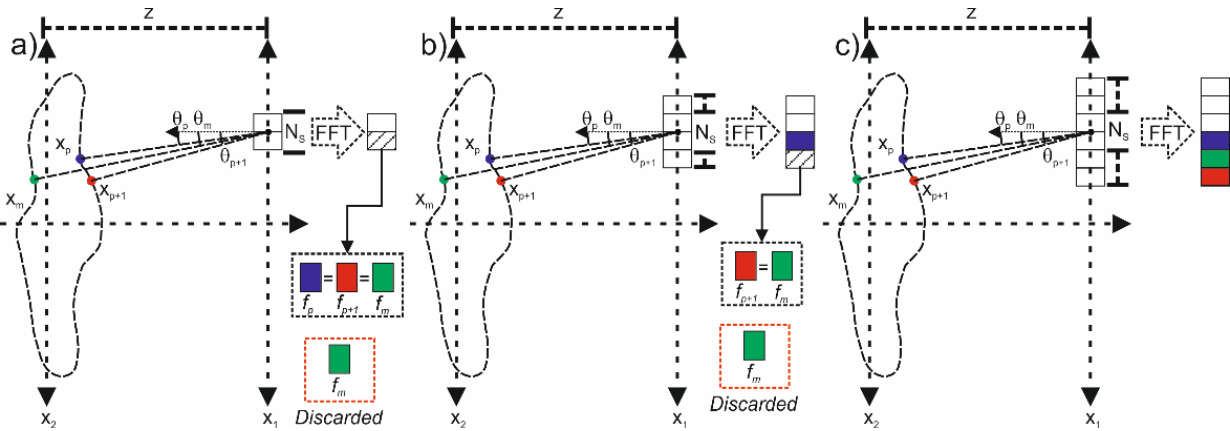


Figure 3. Allocation of discrete frequencies in the PAS algorithm: (a) small segment, (b) medium segment, and (c) large segment.

With the aim to calculate the maximum segment size that enables occlusion, let's consider a set of points that are distributed in the plane (x_2, z). Then, adjacent points x_p and x_{p+1} and an arbitrary hologram segment with center at x_n^c are chosen. The difference between corresponding local frequencies is given by

$$f_{(p+1)xn} - f_{pxn} = \frac{\sin \theta_{(p+1)xn} - \sin \theta_{pxn}}{\lambda}. \quad (9)$$

Note that $\theta_{(p+1)nx} = \theta_{px} + \Delta\theta$, where $\Delta\theta$ is the angular difference between adjacent sources. To eliminate any gap between adjacent frequencies, the right-hand side of Equation (9) must be equal or smaller than the frequency sampling of the segment. This can be expressed as

$$\frac{1}{N_s \Delta} \geq \left| \frac{2 \sin(\Delta\theta/2) \cos(\theta_{pxn} + \Delta\theta/2)}{\lambda} \right|. \quad (10)$$

The denominator on the right-hand side of Equation (10) has been obtained by using the sum-to-product identity. When meeting this condition, the two wavefronts corresponding to the discrete frequencies f_{pxn} and $f_{(p+1)xn}$ are occupying two adjacent discrete locations in the frequency matrix. When considering a back point x_m , which view angle θ_m lies between θ_p and θ_{p+1} , the holographic information associated with the frequency f_{mxn} can be accommodated into the nearest neighbor f_{pxn} or $f_{(p+1)xn}$. Nevertheless, the contribution from f_{mxn} can be disregarded since the frequency positions are already occupied by the front point sources, as shown in Figure 3b. Finally, maximum segment size can be found by solving Equation (10) for N_s , which yields

$$N_s < \frac{\lambda}{2\Delta} |\sin(\Delta\theta/2) \cos(\theta_{pxn} + \Delta\theta/2)|^{-1}. \quad (11)$$

Notably, Equation (11) allows calculating the segment size that enables occlusion culling of back points. Once the occlusion culling of back points is complete, inverse FT is applied, and thus, the hologram segment with the proper depth perspective is obtained.

It is important to differentiate two cases in the occlusion culling. The first case can be exemplified by Figure 3a. In this case, a small segment is employed for the occlusion. As depicted in this figure, the holographic information of two sources (or more) is allocated in

the same frequency pixel. This means that resolution between the sources is lost. Thus, the smaller the segment is, the smaller the resolution in the CGH. On the other hand, when the chosen segment size is closer to N_s , wavefront information of the sources is placed in different frequency pixels, as presented in Figure 3b, which allows preserving resolution in the reconstructed image. Finally, it is important to note that position of the segment shifts allocation of the discrete frequencies but not the condition imposed by Equation (11). For segments that are too far from the center of the CGH, the shifting causes discrete frequencies to fall outside from the frequency support Δ^{-1} .

Visualization of the occlusion culling for a segment in the frequency domain is presented in Figure 4. The employed object is a point cloud of a gargoyle figurine with dimensions 1055 mm (height) \times 971 mm (width) \times 485 mm (depth) composed of approximately 24M points with a density of 9 points/mm². The distance from the center of the object to the hologram plane is one meter. Employed features allow calculating an average angular spacing of 0.038°. Employed features allow calculating an average angular spacing of 0.035°. When employing, $\Delta = 0.62 \mu\text{m}$ and $\lambda = 640 \text{ nm}$, which enables maximum angle view of 62.5°, it is found that N_s must be smaller than 1550 pixels. Thus, segment size is selected as $N_s = 1024$. The size of the calculated CGH is chosen as 4096 \times 4096 pixels. In terms of the PAS technique, the CGH consists of 4 segments of size $N_s \times N_s$, and thus $N, M = 4$. Figure 4 shows the amplitudes of the segment $m = 1$ and $n = 1$ in the frequency domain. Figure 4a depicts the cloud of points without occlusion. Image shows that back and front points contribute to the holographic information of the segment. Thus, the depth cues are not correctly displayed. Figure 4b shows the cloud of points when applying the proposed occlusion culling based PAS. After the occlusion culling of back points, only the front of the gargoyle is seen, which is the correct observable surface. Later, the cloud of points is rotated 180° and PAS with culling occlusion is applied again. Hence, the back of the gargoyle is obtained. The result is shown in Figure 4c. These examples show that our method can eliminate unwanted back points by using the segmentation properties of the PAS.

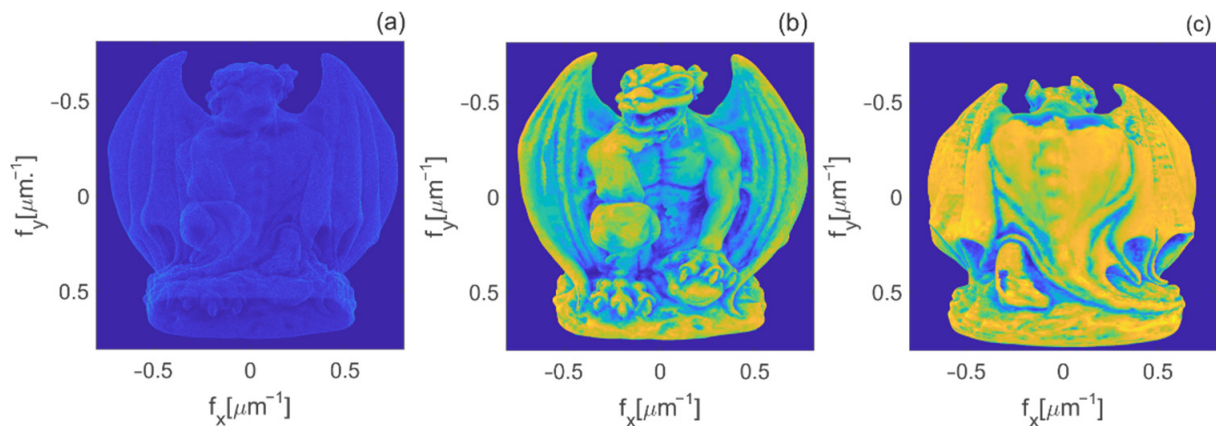


Figure 4. Frequency mapping of the point cloud when using PAS for the segment $m = 1, n = 1$. (a) PAS without occlusion. (b) Front and (c) back of the gargoyle when applying PAS-based occlusion algorithm.

In its basic configuration, the PAS algorithm introduces a truncation error when discretizing the instantaneous local frequencies (Equations (6) and (7)) [32], which decreases the reconstruction quality of the CGH. This truncation error depends on the segment size and can be easily reduced by using a large segment. In the general case of CGH calculation, arbitrarily large segment cannot be selected since the wavefront at the hologram plane may not be well represented. For the proposed occlusion culling PAS, the restriction of the segment becomes stricter due to the limitation imposed with Equation (11). Accurate PAS (A-PAS) can be employed for solving the discretization problem while fulfilling the N_s constraint and sampling theory [31] at the same time. The A-PAS considers that the

segment is enlarged in the discrete frequency domain by an integer factor r . In this way, the frequency sampling is increased r -times, which allows a better approximation of the discrete values of the frequencies to their respective continuous values. After applying the inverse FT to the enlarged segment, the original segment is taken. The A-PAS is implemented in the occluded PAS algorithm by considering that the enlarged segment in frequency domain is not larger than N_s . This means that we must find a hologram segment of size N_{so} and extension factor r such that $N_s > N_{so}r$. When selecting proper N_{so} and r , the accuracy of the PAS algorithm can be reached while preserving the occlusion culling of unwanted back points.

4. Numerical Reconstruction Methods for Wide View-Angle CGHs

With the aim to measure accuracy and quality of the holographic image encoded in the CGH, propagation methods [33,41,42] must be employed. In this section, we investigate two propagation techniques. The first, which is based on the direct integration method [33] is used to assess the accuracy of the CGH calculated by the PAS. The second, that is a generalization of the MFFT-AS technique [10], allows for reconstructing the whole object and visualizing quality of the PAS based occlusion culling.

4.1. Off Axis Direct Integration Method

Recovering the full complex field from wide-angle CGH with classical propagation techniques requires a huge amount of zero padding in x and y directions. Thus, an enormous amount of computational power is required for storing and operating such information. Moreover, the time that is necessary for obtaining the reconstruction will be on the scale of hours or even days. Therefore, it is proposed to employ the integration method [33] for reconstructing a very small off-axis window of the entire complex field. This is done with the aim to carry out a fast quantification of point reproduction quality of calculated CGH.

Off-axis wavefield recovery can be carried out using the Fourier-based solver of the Rayleigh-Sommerfeld integral [43]:

$$u_{out}(x_2, y_2, 0) = \text{IFFT}[\text{FFT}[u_{in}(x_1, y_1, z_R)]\text{FFT}[g(x_2 + x_{OA} - x_1, y_2 + y_{OA} - y_1, -z)]], \quad (12)$$

where $x_2 = x_1 - x_{oa}$, $y_2 = y_1 - y_{oa}$, and (x_{oa}, y_{oa}) are the coordinates of transversal shift, u_{in} is the complex field from the hologram, u_{out} is the reconstructed field, the subindexes 1 and 2 point out the input and output planes, respectively, and

$$g = \frac{\exp(ikD)}{D^2} \left(\frac{1}{D} - ik \right) \quad (13)$$

where $D = \sqrt{x^2 + y^2 + z^2}$. Application of the FFT in Equation (12) generates a circular convolution affecting accuracy of reconstruction. Influence of circular convolution is avoided by increasing twice size of the input matrix by using zero-padding. When solving Equation (12) with these considerations, the desired field is given by the $N_x \times N_y$ lower right submatrix, where N_x is the size of the input field. This method preserves the pixel size between input at output planes. Thus, the size of the integrated window is $x_2 \in (-N_x\Delta/2, N_x\Delta/2)$, $y_2 \in (-N_x\Delta/2, N_x\Delta/2)$. This off-axis direct integration (OADI) method enables fast wavefield reconstruction from any point of view with small amount of memory [33,41,44] but for very small window.

4.2. Multi Fast Fourier Transform Angular Spectrum Method

For the reconstruction of full holographic data from the wide-angle CGH, a generalization of the MFFT-AS method is proposed [10]. The MFFT-AS was initially employed for the reconstruction of Fourier horizontal parallax-DHs (FHPO-DHs) [45], which are small in vertical and large in horizontal directions, respectively. This method applies $(q+1)N_x \times N_y$ FFTs instead of two large FFTs from the classical angular spectrum (AS) method, where N_x ,

N_y are the dimensions of the FHPO-DH and $q = \lfloor B_{y2}/B_{y1} \rfloor$ is the compression factor for y direction (B_{y1} is vertical dimension of the hologram). A critical step in the MFFT-AS is the summation in form of “tiles” in y direction. This makes possible to significantly reduce the computational load. Hence, reconstruction of FHPO-DH with AS is possible. In this work, we extend the MFFT AS application to two dimensions, which allows obtaining accurate reconstruction of full parallax CGH.

Implementation of the MFFT-AS can be described as follows: let O be the 2D object wave of $N_x \times N_y$ samples and spatial dimensions $B_{x1} \times B_{y1}$. We wish to find its diffracted field at plane (x_2, y_2) . The MFFT-AS approach accomplishes this task by calculation of $p \times q$ FFTs as

$$\tilde{O}_1(lp + \alpha, jq + \beta) = \sum_{n=0}^{N_x-1} \sum_{m=0}^{N_y-1} O(n, m) e^{2\pi i(n\alpha/pN_x + m\beta/qN_y)} e^{-2\pi i(nl/N_x + mj/N_y)}, \quad (14)$$

where $p = \lfloor B_{x2}/B_{x1} \rfloor$ is the compression factor in horizontal direction, $lp + \alpha, jq + \beta$ represent the frequency coordinates separated by $1/pB_{x1}$ and $1/qB_{y1}$, respectively. Equation (14) is multiplied by a shifted propagation kernel, which yields

$$\tilde{O}_2(lp + \alpha, jq + \beta) = \tilde{O}_1(lp + \alpha, jq + \beta) e^{-2\pi iz\sqrt{\frac{1}{\lambda^2} - \frac{(lp + \alpha)^2}{(pB_{x1})^2} - \frac{(jq + \beta)^2}{(qB_{y1})^2}}}. \quad (15)$$

It is worth noting that the Equation (15) has size of $N_x p \times N_y q$; however, this large matrix is never allocated. Sequentially, calculated vectors of size $N_x \times N_y$ with Equation (15) are assembled as matrices of the same length $N_x \times N_y$ by next part of the MFFT-AS method. This element of the MFFT-AS is based on the property of FFT that was proposed in references [46] and allows efficient calculations of high-resolution focused wave of small spatial extend. The property enables reduction of bandwidth of FFT without the need of computing FFT of the full-sized vector. To explain the property, let assume a 1D signal A of length qN_y . The method starts with summing up “tiles” as $A_s(n) = \sum_{t=0}^{q-1} A(tq + n)$, where $n \in \{0, \dots, N_y - 1\}$ and then computes FFT. Notably, the \tilde{A}_s is a vector, which contains q -th frequency of \tilde{A}_s . In the 2D MFFT-AS method, the tiling is applied in both directions and the introduced property enables reduction of the sampling rate of the calculated diffracted field. Thus, the result is calculated using at first ‘tiles’ summation method, and then FT as

$$O(n, m) = \sum_{l=0}^{N_x-1} \sum_{s=0}^{p-1} \sum_{j=0}^{N_y-1} \sum_{t=0}^{q-1} \tilde{O}_2(sp + l, tq + j) e^{2\pi i(nl/N_x + mj/N_y)}. \quad (16)$$

Notably, full field reconstruction with the 2D MFFT-AS AS requires $q \times p + 1$ FFTs of size $N_x \times N_y$, and pixel size at the output plane is determined by $\Delta x_2 = p \Delta x_1$, and $\Delta y_2 = q \Delta y_1$.

4.3. Comparison of Full and Small off Axis Window Reconstruction

The strategies based on off axis window and full image reconstruction are here compared from the computational point of view. For this, the set of holograms for reconstruction distance $z = 1000$ mm, pixel count 4096×4096 , and several pixel pitches were generated and reconstructed.

Table 1 presents the image size and the obtained computation times for both reconstruction methods when using selected pixel pitches. Notably, the MFFT-AS enables to obtain image sizes ranging from one quarter of meter up to one meter. However, the price to pay is a large processing time. For example, reconstruction of the smallest pixel pitch ($\Delta = 0.6 \mu\text{m}$) requires almost 12 h of processing. On the other hand, the OADI method provides results in a few seconds for reconstructing the complex field but of window size of a few millimeters.

Table 1. Calculated Field of View and computation time for the off-axis direct integration method and the MFFT-AS, $\lambda = 640$ nm, $z = 1000$ mm.

Δ/FoV	Image Size		Calculation Speed	
	OADI	MFFT-AS	OADI	MFFT-AS
0.6 $\mu\text{m}/62^\circ$	2.5 mm \times 2.5 mm	1.2 m \times 1.2 m	10.5 s	38,300 s
1.2 $\mu\text{m}/31^\circ$	5 mm \times 5 mm	0.54 m \times 0.54 m	10.5 s	1900 s
1.8 $\mu\text{m}/20^\circ$	7.3 mm \times 7.3 mm	0.36 m \times 0.36 m	10.5 s	304 s
2.4 $\mu\text{m}/15^\circ$	9.9 mm \times 9.9 mm	0.26 m \times 0.26 m	10.5 s	104 s

5. Diffraction Efficiency Based on Assessment of CGH Quality

In this section, assessment of CGH quality based on diffraction efficiency measure is carried out. This is done with the aim to quantify quality of point reproduction of calculated CGH. Reconstruction of wide-angle CGHs require, see first row of Table 1, a large amount of memory and processing time. Nevertheless, for measuring the diffraction efficiency of CGHs of this work, we retrieve a small region where a point source is reconstructed. Hence, the OADI method is suitable for measuring the diffraction efficiency of CGHs calculated with the PAS algorithm.

The first diffraction efficiency-based test is evaluated with two CGHs of ten point sources distributed linearly along the diagonal from the center of the image $P_0(0, 0, z)$ up to corner point $P_{10} = (-0.475B_{x2}, -0.475B_{y2}, z)$, where $z = 1000$ mm. Pixel pitch of the CGHs is $\Delta = 0.62 \mu\text{m}$. Theoretical CGH, which is reference one, is calculated using Equation (2), while the second CGH with the PAS algorithm employing $N_{so} = 256$ and $r = 4$. Calculated CGHs are processed with Equation (12) and the corresponding off-axis coordinate. As a result, the single point source with its nearest neighborhood is reconstructed. Figure 5a,b present the reconstruction of point P_{10} of theoretical and PAS CGHs, respectively. Visually, reconstructed point sources have identical profiles and almost the same peak value (P-V). Figure 5c presents the accuracy test in relation to point source position along the diagonal of image space. Maximum amplitude values are normalized with respect to the on-axis point P_0 from theoretical CGH. Regardless, the CGH is made with PAS method or with Equation (2), the linear loss of amplitude due to point source position is present. Moreover, it is clearly seen in the plot that accuracy of reconstructed point sources is strongly related to the selection of the parameter r , e.g., for $r \geq 3$, the maximum amplitude of each point starts to behave stable and is close to the result of theoretical CGH. Accordingly, CGHs of high accuracy made with PAS can be achieved by using a value N_{so} and large r . Nevertheless, the constraint provided by Equation (11) must be fulfilled all the time if occlusion culling is desired. For this reason, we perform a test that is aimed to measure the accuracy of calculated CGHs with the PAS with different parameters N_{so} and r . As a measure of accuracy, the ratio of maximum amplitude of reconstructed point P_{10} between PAS and theoretical CGH is used. Corresponding results are shown in Figure 6a. The obtained ratios demonstrate that when using original segment size ($r = 1$), the diffraction efficiency is low and unstable, which means that calculated CGH with PAS is not optimal. When using large values of r ($r > 2$), the maximum amplitude increases its value independently of the N_{so} , which is pointed out by large dash box into the plot.

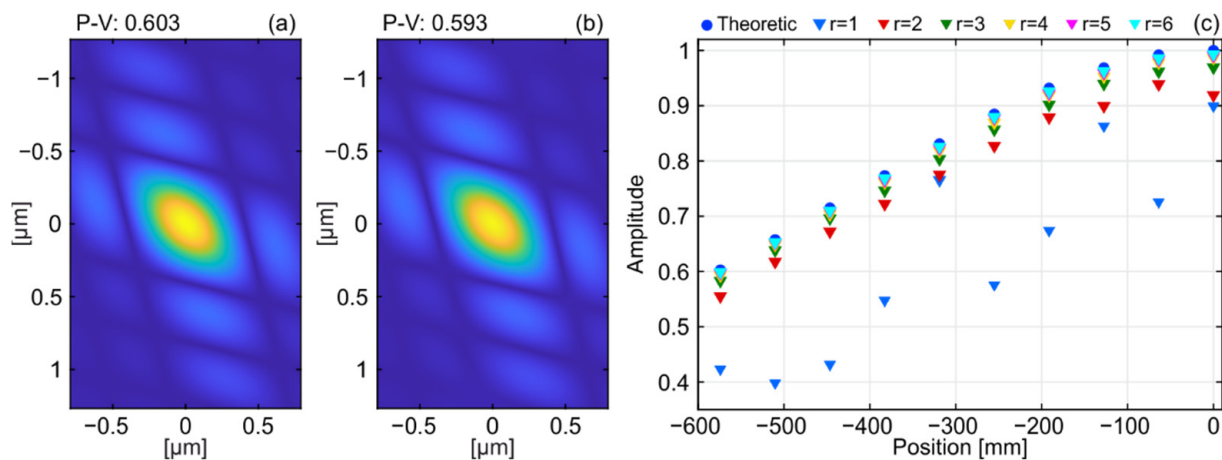


Figure 5. Evaluation of off-axis single point reconstructions with the OADI method; (a) Reconstructed amplitude of the point source P_{10} from theoretical CGH; (b) Reconstructed amplitude of the point source P_{10} from PAS CGH; and (c) normalized reconstructed amplitudes for several N_{so} and r .

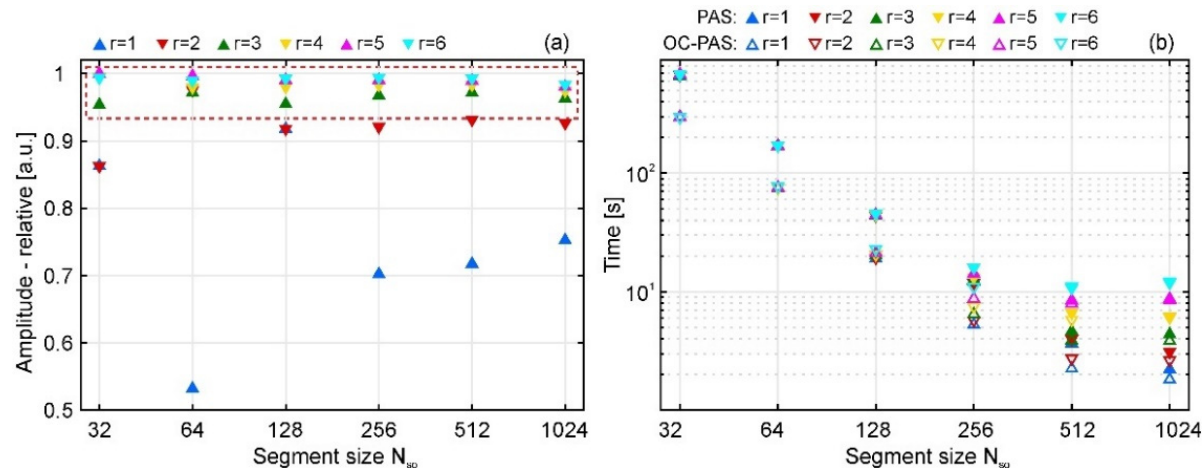


Figure 6. (a) Normalized reconstructed amplitude of P_{10} for different N_{so} and r ; (b) Reconstruction time for a CGH of 1 million points for different segment N_{so} and factors r without (PAS) and with (OC-PAS) occlusion culling.

The second test is carried out for measuring the computation time of calculated CGH with a point cloud of one million points. The cloud has a similar point density to the gargoyle figurine presented in Section 3. Different N_{so} and r values without and with occlusion culling routine are employed. The results are presented in Figure 6b. Note that PAS calculation of a segment consists of two parts: allocation of holographic information according to the local instantaneous discrete frequencies and performing FFT. Time consumption for allocation depends on the number of points, and thus the larger the cloud is, the larger the computational effort. Time consumption is particularly demanding when the number of points within the cloud is counted in millions. In comparison, the computational effort of the FFT only depends on the size of the frequency matrix ($N_{so} \times r$), where the holographic information is stored. Since the computational complexity of FFT is given by $(N_{so} \times r) \times \log(N_{so} \times r)$, then a small product of N_{so} and r will result in a short computation time, which is almost negligible, while a large product between N_{so} and r , will increase it. However, this FFT-related time is still shorter than for point processing. A benefit of using large segments N_{so} is that less segments are computed for hologram generation, which speeds up the CGH computation. When measuring time for the occlusion culling, it is seen that the occlusion PAS is faster than normal PAS. For example, generation of the CGH without occlusion for $N_{so} = 32$ and $r = 3$, and $N_{so} = 512$ and

$r = 3$ took around 674 and 4.6 s, respectively. On the other hand, calculation of the CGH with occlusion for previous parameters took around 297 s and 3.9 s, respectively. Notably, for segments of size $N_{so} \times r$ that do not fulfill Equation (11) the growth of computation time is higher for the occlusion culling than for the computation without occlusion. This is because of the finer frequency sampling of the segment, which means that back points are allowed to store their holographic information. Therefore, the number of processed points grows, and thus the computation time as well.

As discussed in former paragraph, selection of N_{so} and r for ensuring high accuracy and fast execution time must consider the constraint imposed by Equation (11). However, Equation (11) relies in the angular spacing $\Delta\theta$. The parameter $\Delta\theta$ depends on the geometry of the object, the dimension of the hologram, and the separation between object and hologram planes. Due to the mentioned features, the estimation of the angular spacing is a non-trivial issue. Here, it is decided to estimate the local angular spacing with the fitting of a Gaussian distribution to the computed local density of points. Also, considering the standard deviations, we estimate the quasi-minimal angular spacing value for the points clouds that statistically work properly for over 99% of the object surface. Table 2 presents the connection between the average angular spacing of the point cloud and the proper segment size N_{so} as it is stated in Equation (11). Four point clouds with the same geometry from gargoyle figure from Section 3 are employed. These clouds have 200 thousand, 1 million, 5 million, and 24 million of points. Investigation of these exemplary point clouds presents the proper choice of the segment size due to the point cloud angular spacing and their respective CGH time calculation.

Table 2. Calculated segment size respect to the average point cloud angular spacing for neighboring points and computation time of CGH-PAS without and with occlusion culling.

	200 Thousand	1 Million	5 Million	24 Million
Local angular spacing	0.4051°	0.1806°	0.0821°	0.035°
N_s —Equation (11)	146	329	723	1563
N_{so} ($r = 1$)	128	256	512	1024
PAS without OC	7.7 s	9.4 s	14.0 s	31.0 s
PAS with OC	4.5 s	6.1 s	8.9 s	20.5 s

6. Reconstruction of Wide-Angle CGHs Calculated with the Occlusion Culling Based-PAS Algorithm

In this section, numerical and optical reconstructions of wide-angle CGHs obtained with the occlusion culling based PAS are carried out. PAS algorithm is implemented in Matlab software, which is installed on a PC equipped with Intel i9-9900K processor, 32 GB of RAM, and run without support of GPU. Selected size of the CGHs is 4160×2160 pixels, which corresponds to the size of the 4K SLM Holoeye GAEA 2.0, pixel pitch $\Delta_{SLM} = 3.74 \mu\text{m}$. CGHs are calculated from the cloud of 24 million points defined in Section 3 and PAS parameters: $N_{so} = 512$, $r = 3$, and $\Delta = 0.62 \mu\text{m}$, which according to Table 2 fulfills N_s limit. Calculation time for each CGH is around 190 s, which can be reduced up to 30 s when using the Matlab parallel toolbox. When comparing this time with Table 1 from reference [29], it can be seen that our approach improves the calculation time by a factor of 3000.

Figure 7a–c show numerical reconstructions for three perspectives angles: 0°, 45°, and 180° of CGH calculated with the 2D MFFT-AS, respectively. Notably, the application of the occlusion culling based PAS algorithm allows eliminating unwanted back points, and hence, reconstruction of the object with proper depth cues. It is worth noting that SFI method is not able to provide any of the presented results since it is a method designed under the constraints of the paraxial regime. Video S1 presents the numerical reconstruction of the gargoyle view angles from 0° to 360°. The cloud of points was rotated 8° between each frame.

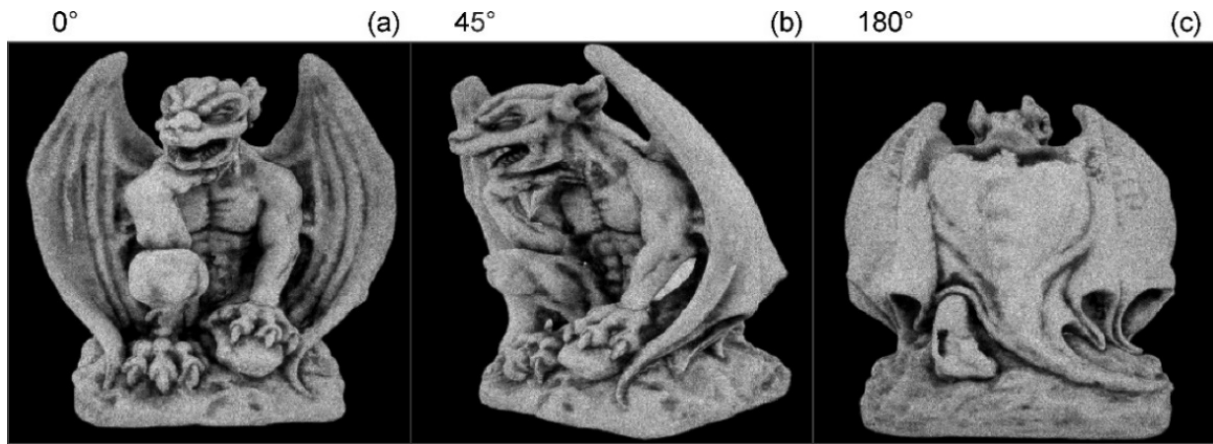


Figure 7. 2D MFFT AS reconstructions for different perspective angles: (a) 0° , (b) 45° , and (c) 180° .

Optical reconstruction of CGH is carried out in the display setup presented in Figure 8. Illumination laser source ($\lambda_R = 640$ nm) hits half-wave plate (HWP), which controls polarization state. Next, the beam passes through microscopic objective (MO) and a pinhole (PH), generating a spherical wavefront. A collimator lens C ($F_c = 300$ mm) is placed in front of the pinhole to obtain an extended plane wave. Plane wave illumination is directed to the phase only 4K SLM by a non-polarized beam splitter. SLM is imaged by an afocal demagnifying system composed of an objective ($F_1 = 200$ mm, $\mathcal{O}_1 = 50$ mm) and an eyepiece ($F_2 = 33$ mm, $\mathcal{O}_2 = 25$ mm). At the viewing window (VW) plane pixel pitch of the image of SLM is $\Delta'_{\text{SLM}} = F_2/F_1 \times \Delta_{\text{SLM}} = 0.62$ μm . The small pixel pitch allows for a wide viewing angle (62.5°). However, the physical aperture of the eyepiece limits it to 36° .

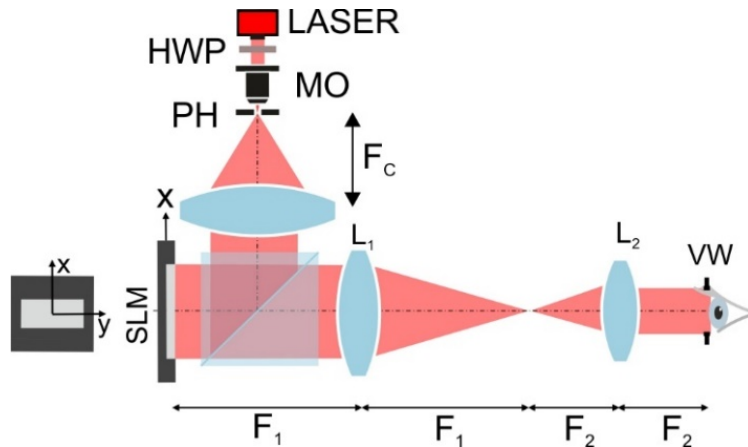


Figure 8. Scheme of wide-angle holographic display used for CGH optical reconstruction.

Figure 9 shows optical reconstructions of CGH generated and reconstructed for four view angles: 0° , 45° , 180° and 275° . To fit the viewing angle of the display system, gargoyle dimensions are resized to $559 \times 527 \times 279$ [mm^3]. Since the dimension of the cloud is reduced, the average angular spacing of the point cloud decreases to 0.030° . For this value, the N_S must be smaller than 1900 pixels. Hence, former PAS parameters fulfill accuracy and speed for CGH calculation as well. Obtained results prove that the occlusion culling based-PAS can eliminate unwanted back points for each angle. Video S2 presents the optical reconstruction of the gargoyle from 0° to 360° . Here, the cloud of points was rotated 1° per frame.

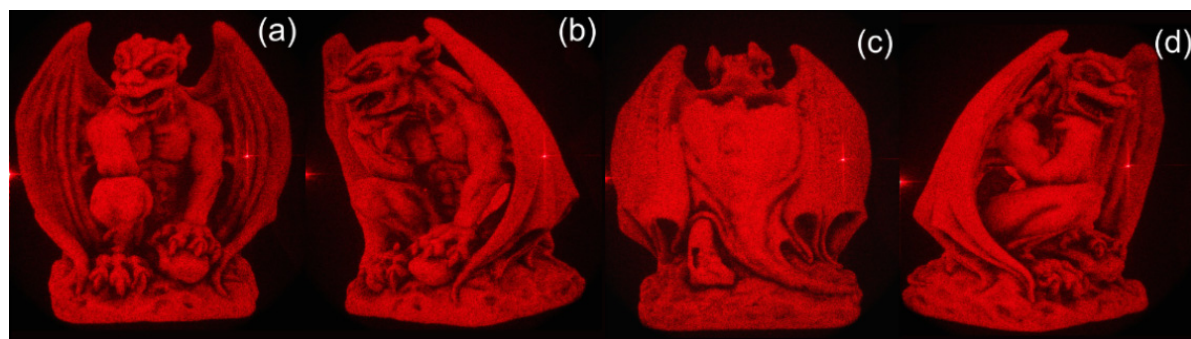


Figure 9. Optical reconstructions of CGHs generated with culling-occlusion-PAS-based algorithm for different view angles: (a) 0° , (b) 45° , (c) 180° , and (d) 275° .

7. Conclusions

In this work, we proposed a simple, effective and fast occlusion culling strategy for wide-angle view holograms. Our approach takes advantage of PAS algorithm, which is based on mapping of 3D object information from spatial to frequency domain. It is shown that optimal segment size that enables occlusion of back points can be calculated according to the average angular spacing of the point cloud. Moreover, sorting of the cloud of points in the z-axis allows ordering the point sources from the nearest to the farthest respect to the hologram plane. In this way, sources that are closer to the hologram plane are labeled as front ones and allocate their holographic information into the frequency matrix first. Other point sources of the same frequency but farther from the hologram plane are labeled as back ones, and thus, their information into the frequency matrix is omitted. Moreover, two methods for numerical reconstruction of wide-angle view CGH were studied. The first was the OADI method, which allows reconstructing a small window from the whole image space. In this way, efficient numerical technique is obtained, which enables measuring the diffraction efficiency of the PAS algorithm. The second was the 2D MFFT-AS, which allows reconstructing the full image space. It was employed for reconstructing the whole object and visualize the quality of the occlusion culling that was carried out with the PAS. Finally, optical reconstruction of occluded CGHs in wide-angle holographic display verified the validity of our occlusion culling strategy. Notably, our methodology enables fast computation time for obtaining occluded CGHs from very large point clouds.

Supplementary Materials: The following are available online at <https://www.mdpi.com/article/10.3390/photonics8080298/s1>; Video S1: The numerical reconstruction of the gargoyle view angles from 0° to 360° ; Video S2: The optical reconstruction of the gargoyle from 0° to 360° .

Author Contributions: Conceptualization and methodology, J.M.-C.; software, R.K.; experimental validation, M.C. and M.S.I.; supervision, T.K. All authors have read and agreed to the published version of the manuscript.

Funding: This research was funded by National Science Centre, Poland grant number UMO-2018/31/B/ST7/02980.

Institutional Review Board Statement: Not applicable.

Informed Consent Statement: Not applicable.

Data Availability Statement: Data underlying the results presented in this paper are publicly available at this time but may be obtained from the authors upon request.

Acknowledgments: The authors would like to thank to the Warsaw University of Technology for the statutory funds provided to this research.

Conflicts of Interest: The authors declare no conflict of interest.

References

- Yamaguchi, M. Full-Parallax Holographic Light-Field 3-D Displays and Interactive 3-D Touch. *Proc. IEEE* **2017**, *105*, 947–959. [[CrossRef](#)]
- Bove, V.M. Display holography’s digital second act. *Proc. IEEE* **2012**, *100*, 918–928. [[CrossRef](#)]
- Kim, M.K. Principles and techniques of digital holographic microscopy. *SPIE Rev.* **2010**, *1*, 1–50. [[CrossRef](#)]
- Dong, J.; Jiang, C.; Jia, S. Digital holographic metrology based on multi-angle interferometry. *Opt. Lett.* **2016**, *41*, 4301. [[CrossRef](#)]
- Grujić, D.; Vasiljević, D.; Pantelić, D.; Tomić, L.; Stamenković, Z.; Jelenković, B.; Zhang, W.; Zhang, D.; Vukmirović, N.; Stepanenko, D. Naturally safe: Cellular noise for document security. *J. Biophotonics* **2019**, *12*, 1–9.
- Khan, G.S.; Mantel, K.; Harder, I.; Lindlein, N.; Schwider, J. Design considerations for the absolute testing approach of aspherics using combined diffractive optical elements. *Appl. Opt.* **2007**, *46*, 7040–7048. [[CrossRef](#)] [[PubMed](#)]
- Zhang, H.; Zhao, Y.; Cao, L.; Jin, G. Fully computed holographic stereogram based algorithm for computer-generated holograms with accurate depth cues. *Opt. Express* **2015**, *23*, 3901–3913. [[CrossRef](#)]
- Lee, S.; Jo, Y.; Yoo, D.; Cho, J.; Lee, D.; Lee, B. Tomographic near-eye displays. *Nat. Commun.* **2019**, *10*, 1–10. [[CrossRef](#)]
- Kozacki, T.; Martinez-Carranza, J.; Kukolowicz, R.; Finke, W. Accurate reconstruction of horizontal parallax-only holograms by angular spectrum and efficient zero-padding. *Appl. Opt.* **2020**, *59*, 8450–8458. [[CrossRef](#)]
- Isomae, Y.; Shibata, Y.; Ishinabe, T.; Fujikake, H. Design of 1-μm-pitch liquid crystal spatial light modulators having dielectric shield wall structure for holographic display with wide field of view. *Opt. Rev.* **2017**, *24*, 165–176. [[CrossRef](#)]
- Higashida, R.; Funabashi, N.; Aoshima, K.; Miura, M.; Machida, K. Diffraction of light using high-density magneto-optical light modulator array. *Opt. Eng.* **2020**, *59*, 1–13. [[CrossRef](#)]
- Buckley, E. Holographic projector with one lens. *Opt. Lett.* **2010**, *35*, 3399–3401. [[CrossRef](#)]
- Blinder, D.; Chlipala, M.; Kozacki, T.; Schelkens, P. Photorealistic computer generated holography with global illumination and path tracing. *Opt. Lett.* **2021**, *46*, 2188–2191. [[CrossRef](#)]
- Wakunami, K.; Yamashita, H.; Yamaguchi, M. Occlusion culling for computer generated hologram based on ray-wavefront conversion. *Opt. Express* **2013**, *21*, 21811–21822. [[CrossRef](#)]
- Matsushima, K.; Nakahara, S. Extremely high-definition full-parallax computer-generated hologram created by the polygon-based method. *Appl. Opt.* **2009**, *48*, H54–H63. [[CrossRef](#)] [[PubMed](#)]
- Zhang, H.; Cao, L.; Jin, G. Computer-generated hologram with occlusion effect using layer-based processing. *Appl. Opt.* **2017**, *56*, F138–F143. [[CrossRef](#)]
- Yeom, H.-J.; Park, J.-H. Calculation of reflectance distribution using angular spectrum convolution in mesh-based computer generated hologram. *Opt. Express* **2016**, *24*, 19801–19813. [[CrossRef](#)]
- Chen, R.H.Y.; Wilkinson, T.D. Computer generated hologram from point cloud using graphics processor. *Appl. Opt.* **2009**, *48*, 6841–6850. [[CrossRef](#)]
- Chen, R.H.Y.; Wilkinson, T.D. Computer generated hologram with geometric occlusion using GPU-accelerated depth buffer rasterization for three-dimensional display. *Appl. Opt.* **2009**, *48*, 4246–4255. [[CrossRef](#)] [[PubMed](#)]
- Symeonidou, A.; Blinder, D.; Munteanu, A.; Schelkens, P. Computer-generated holograms by multiple wavefront recording plane method with occlusion culling. *Opt. Express* **2015**, *23*, 22149–22161. [[CrossRef](#)]
- Hong, J.; Kim, Y.; Choi, H.J.; Hahn, J.; Park, J.H.; Kim, H.; Min, S.-W.; Chen, M. Three-dimensional display technologies of recent interest: Principles, status, and issues. *Appl. Opt.* **2011**, *50*, 87–115. [[CrossRef](#)] [[PubMed](#)]
- Gilles, A.; Gioia, P.; Cozot, R.; Morin, L. Complex modulation computer-generated hologram with occlusion effect by a fast hybrid point-source/wave-field approach. In Proceedings of the 2015 Conference: Pacific Conference on Graphics and Applications, Beiging, China, 7–9 October 2015; pp. 1–9.
- Askari, M.; Kim, S.-B.; Shin, K.-S.; Ko, S.-B.; Kim, S.-H.; Park, D.-Y.; Yu, Y.-G.; Park, J.-H. Occlusion handling using angular spectrum convolution in fully analytical mesh-based computer generated hologram. *Opt. Express* **2017**, *25*, 25867–25878. [[CrossRef](#)]
- Chen, J.-S.; Chu, D.P. Improved layer-based method for rapid hologram generation and real-time interactive holographic display applications. *Opt. Express* **2015**, *23*, 18143–18155. [[CrossRef](#)] [[PubMed](#)]
- Kang, H.; Stoykova, E.; Yoshikawa, H. Fast phase-added stereogram algorithm for generation of photorealistic 3D content. *Appl. Opt.* **2016**, *55*, A135–A143. [[CrossRef](#)]
- Shimobaba, T.; Masuda, N.; Ito, T. Simple and fast calculation algorithm for computer-generated hologram with wavefront recording plane. *Opt. Lett.* **2009**, *34*, 3133–3136. [[CrossRef](#)]
- Liu, S.; Wei, H.; Li, N.; Liu, Z.; Zhang, J. Occlusion calculation algorithm for computer generated hologram based on ray tracing. *Opt. Commun.* **2019**, *443*, 76–85. [[CrossRef](#)]
- Zhao, K.; Huang, Y.; Yan, X.; Jiang, X. Occlusion culling and calculation for a computer generated hologram using spatial frequency index method. *J. Opt.* **2015**, *17*, 1–9. [[CrossRef](#)]
- Yamaguchi, M.; Hoshino, H.; Honda, T.; Ohya, N. Phase-Added Stereogram: Calculation of Hologram Using Computer Graphics Technique. In Proceedings of the 1993 Conference: Practical Holography VII: Imaging and Materials, San Jose, CA, USA, 17 September 1993; pp. 25–31.
- Kang, H.; Yamaguchi, T.; Yoshikawa, H. Accurate phase-added stereogram to improve the coherent stereogram. *Appl. Opt.* **2008**, *47*, D44–D54. [[CrossRef](#)]

31. Kang, H. Compensated phase-added stereogram for real-time holographic display. *Opt. Eng.* **2007**, *46*, 1–11. [[CrossRef](#)]
32. Shen, F.; Wang, A. Fast-Fourier-transform based numerical integration method for the Rayleigh-Sommerfeld diffraction formula. *Appl. Opt.* **2006**, *45*, 1102–1110. [[CrossRef](#)]
33. Leseberg, D.; Frère, C. Computer-generated holograms of 3-D objects composed of tilted planar segments. *Appl. Opt.* **1988**, *27*, 3020–3024. [[CrossRef](#)] [[PubMed](#)]
34. Yatagai, T. Stereoscopic approach to 3-D display using computer-generated holograms. *Appl. Opt.* **1976**, *15*, 2722–2729. [[CrossRef](#)]
35. Tang, C.; Yao, B. Fast computation for generating CGH of a 3D object by employing connections between layers. *J. Mod. Opt.* **2012**, *59*, 1406–1409. [[CrossRef](#)]
36. Shimobaba, T.; Kakue, T.; Ito, T. Review of Fast Algorithms and Hardware Implementations on Computer Holography. *IEEE Trans. Ind. Inform.* **2016**, *12*, 1611–1622. [[CrossRef](#)]
37. Zhao, Y.; Cao, L.; Zhang, H.; Kong, D.; Jin, G. Accurate calculation of computer-generated holograms using angular-spectrum layer-oriented method. *Opt. Express* **2015**, *23*, 25440–25449. [[CrossRef](#)] [[PubMed](#)]
38. Ju, Y.-G.; Park, J.-H. Foveated computer-generated hologram and its progressive update using triangular mesh scene model for near-eye displays. *Opt. Express* **2019**, *27*, 23725–23738. [[CrossRef](#)] [[PubMed](#)]
39. Katz, S.; Tal, A.; Basri, R. Direct visibility of point sets. *ACM Trans. Graph.* **2007**, *26*, 1–11. [[CrossRef](#)]
40. Veerman, J.A.C.; Rusch, J.J.; Urbach, H.P. Calculation of the Rayleigh-Sommerfeld diffraction integral by exact integration of the fast oscillating factor. *J. Opt. Soc. Am. A* **2005**, *22*, 636–646. [[CrossRef](#)]
41. Kozacki, T.; Falaggis, K.; Kujawinska, M. Computation of diffracted fields for the case of high numerical aperture using the angular spectrum method. *Appl. Opt.* **2012**, *51*, 7080–7088. [[CrossRef](#)] [[PubMed](#)]
42. Matsushima, K. Shifted angular spectrum method for off-axis numerical propagation. *Opt. Express* **2010**, *18*, 18453–18463. [[CrossRef](#)] [[PubMed](#)]
43. Zhang, W.; Zhang, H.; Matsushima, K.; Jin, G. Shifted band-extended angular spectrum method for off-axis diffraction calculation. *Opt. Express* **2021**, *29*, 10089–10103. [[CrossRef](#)]
44. Kozacki, T.; Finke, G.; Garbat, P.; Zaperty, W.; Kujawińska, M. Wide angle holographic display system with spatiotemporal multiplexing. *Opt. Express* **2012**, *20*, 27473–27481. [[CrossRef](#)] [[PubMed](#)]
45. Kanka, M.; Wuttig, A.; Graulig, C.; Riesenbergs, R. Fast exact scalar propagation for an in-line holographic microscopy on the diffraction limit. *Opt. Lett.* **2010**, *35*, 217–219. [[CrossRef](#)] [[PubMed](#)]
46. Hillenbrand, M.; Hoffmann, A.; Kelly, D.P.; Sinzinger, S. Fast nonparaxial scalar focal field calculations. *J. Opt. Soc. Am. A* **2014**, *31*, 1206–1214. [[CrossRef](#)]